

# **Photoinduced concurrent intralayer and interlayer structural transitions and associated topological transitions in $M\text{Te}_2$ ( $M=\text{Mo}, \text{W}$ )**

Yingpeng Qi<sup>1,3,5\*</sup>, Mengxue Guan<sup>2,5</sup>, Daniela Zahn<sup>1</sup>, Thomas Vasileiadis<sup>1</sup>, H el ene Seiler<sup>1</sup>, Yoav William Windsor<sup>1</sup>, Hui Zhao<sup>2</sup>, Sheng Meng<sup>2,4\*</sup>, Ralph Ernstorfer<sup>1\*</sup>

<sup>1</sup>Fritz-Haber-Institut der Max-Planck-Gesellschaft, Faradayweg 4-6, Berlin 14195, Germany

<sup>2</sup>Beijing National Laboratory for Condensed Matter Physics and Institute of Physics, Chinese Academy of Sciences, Beijing 100190, P. R. China

<sup>3</sup>Center for Ultrafast Science and Technology, School of Physics and Astronomy, Shanghai Jiao Tong University, 200240 Shanghai, China

<sup>4</sup>School of Physical Sciences, University of Chinese Academy of Sciences, Beijing 100049, China

<sup>5</sup>These authors contributed equally: Yingpeng Qi, Meng-Xue Guan

\*Correspondence to [qiyp@sjtu.edu.cn](mailto:qiyp@sjtu.edu.cn), [smeng@iphy.ac.cn](mailto:smeng@iphy.ac.cn) and [ernstorfer@fhi-berlin.mpg.de](mailto:ernstorfer@fhi-berlin.mpg.de)

Manipulating crystal structure and the corresponding electronic properties in topological quantum materials provides opportunities for the exploration of exotic physics and practical applications. As prototypical topological materials, the bulk  $\text{MoTe}_2$  and  $\text{WTe}_2$  are identified to be Weyl semimetals and higher-order topological insulators. The non-centrosymmetric interlayer stacking in  $\text{MoTe}_2$  and  $\text{WTe}_2$  causes the Weyl semimetal phase while the intralayer Peierls distortion causes the higher-order topological insulator phase. Here, by ultrafast electron diffraction and TDDFT-MD simulations, we report the photoinduced concurrent intralayer and

interlayer structural transitions in both the low temperature Td and room temperature 1T' phase of MoTe<sub>2</sub> and WTe<sub>2</sub>. The ultrafast reduction of the intralayer Peierls distortion within 0.3 ps is demonstrated to be driven by Mo-Mo (W-W) bond stretching and dissociation. Both the interlayer shear displacement and the suppression of the intralayer Peierls distortion are identified to be caused by photon excitation, which is a different mechanism compared to the THz field and optical field driven structural transitions reported previously. The revealed intralayer and interlayer structural transitions, provide an ultrafast switch from the rich topological nontrivial phases, such as the Weyl semimetal phase and (higher-order) topological insulator phase, to trivial phase in bulk MoTe<sub>2</sub> and WTe<sub>2</sub> and most monolayer TMDCs. Our work elucidates the pathway of the intralayer and interlayer structural transitions and the associated topological switches in atomic and femtosecond spatiotemporal scale, and sheds light on new opportunities for the ultrafast manipulation of topological and other exotic properties by photon excitation.

## **Introduction**

Within the transition metal dichalcogenides (TMDCs) family, MoTe<sub>2</sub> and WTe<sub>2</sub> have recently sparked broad research interest for their rich structural phases and unusual electronic structures, such as the semiconductor-to-semimetal structural transition [1, 2], extremely large magnetoresistance [2, 3], quantum spin Hall effect

[4-7], and novel topological phases [8-14]. At room temperature, MoTe<sub>2</sub> is in its 1T' phase and forms a layered structure with double sheets of Te atoms bound together by interleaving Mo atoms, as shown in Fig. 1a. By lowering the temperature below 250 K, bulk MoTe<sub>2</sub> undergoes a structural transition from the monoclinic 1T' to the orthorhombic Td phase. These two semimetallic phases hold distinct interlayer stacking while both exhibit the same intralayer crystal structure with a Peierls distortion [2]. The intralayer Peierls distortion is characterized by the Mo-Mo metal bonds, which modulate the adjacent Mo atoms by alternating shorter and longer distances along the *b* axis, as well as the out-of-plane wrinkling of the Te atoms as shown in Fig. 1a. The 1T' phase of MoTe<sub>2</sub> belongs to the centrosymmetric space group (P2<sub>1</sub>/m), and the Td phase of MoTe<sub>2</sub> belongs to the non-centrosymmetric space group (Pmn2<sub>1</sub>). As a sister compound of MoTe<sub>2</sub>, WTe<sub>2</sub> has commonly been observed in the Td phase, even in a high temperature. Both the 1T' and Td phase of MoTe<sub>2</sub> and WTe<sub>2</sub> are topological nontrivial. The bulk Td phase is a type-II Weyl semimetal [8-12, 15] and the bulk 1T' and Td phases are higher-order topological insulators [13, 14, 16]. The monolayers of MoTe<sub>2</sub> and WTe<sub>2</sub> are topological insulators [2, 4, 5, 17].

The crystalline topological phase of electrons is intrinsically protected by the symmetry of the crystal [18-21]. Therefore, triggering an intralayer or interlayer symmetry change offers prospects in practical applications such as topological switch electronics. An ultrafast switching of the Weyl semimetal phase of WTe<sub>2</sub> to the trivial semimetal phase via an interlayer stacking transition can be achieved by an intense THz field pump [22]. The excitation of the coherent interlayer shear phonon mode is

attributed to the electric field driving electron transfer from the topmost valence band to the conduction band. Under an infrared (800 nm) and a midinfrared (2600 nm) laser pump [23], a topological switch in the Td phase of MoTe<sub>2</sub>, analogous to the THz pump induced switching in WTe<sub>2</sub> [22], was observed within 0.7 ps through spectroscopic measurements. The recent angle-resolved photoemission spectroscopy (ARPES) study [24] on the Td phase of WTe<sub>2</sub> shows that, at 800 nm and a low excitation density, the shear mode induced photoemission intensity oscillation can be described by a  $\pi$ -shifted sine function, implying an impulsive excitation of this shear mode by the laser field. However, a direct observation of the laser-induced ultrafast interlayer stacking transition with a structural probe has not been reported yet.

The intralayer Peierls distortion is an intrinsic structural character of the 1T' and Td phase of MoTe<sub>2</sub>, WTe<sub>2</sub> and their monolayer counterparts [2], caused by Fermi surface nesting. It brings about the onset of unique physical phenomena, such as unprecedented anisotropic optical and electronic properties [25]. More importantly, the intralayer distortion induces the band inversion and causes monolayers of MoTe<sub>2</sub> and WTe<sub>2</sub> to become topological insulators [2, 4, 5, 17] and the bulk to become a higher-order topological insulator [13, 14, 16]. A schematic illustration of the band inversion in monolayer 1T' MoTe<sub>2</sub> is shown in Fig. 1b. With the inclusion of spin-orbit coupling (SOC), the band hybridization and the lifting of degeneracies at the Dirac cones formed by the band inversion open a bandgap in the bulk states [2, 4, 5]. The topological band inversion and the bandgap opening are the hallmarks of a quantum spin Hall state in monolayer 1T' WTe<sub>2</sub> and MoTe<sub>2</sub> [4-7]. Therefore, a

dynamical control of the intralayer Peierls distortion will modulate the topological and exotic electronic properties in MoTe<sub>2</sub> and WTe<sub>2</sub>.

Here we report a comprehensive study of the ultrafast structural response in the 1T' and the Td phase of MoTe<sub>2</sub> and WTe<sub>2</sub> induced by 550 nm and 2000 nm laser excitation. We identify concurrent interlayer and intralayer structural transitions, i.e. the interlayer shear displacement and the reduction of intralayer Peierls distortion, by ultrafast electron diffraction (UED) supported by TDDFT-MD simulations. The interlayer shear mode in the Td phase, which is a signature of the Weyl semimetal phase to trivial phase transition, is observed in the ultrafast electron diffraction experiments as an oscillation of Bragg reflection intensities. It is well described by a  $\pi$ -shifted cosine function indicating a displacive excitation of this coherent phonon mode, so the interlayer structural transition is driven by electron-phonon coupling which is distinct from the laser field driven transition based on ultrafast spectroscopy measurements. An ultrafast Mo-Mo (W-W) bond stretching in both the 1T' and the Td phase is revealed as an anisotropic changes of Bragg reflections within 0.3 ps. It triggers an ultrafast reduction of intralayer Peierls distortion and a transition from the higher-order topological insulator phase in bulk 1T' and Td phase to the trivial phase. Since the stable phase of most monolayer TMDCs is the 1T' phase, we expect that the transition from the topological insulator phase to the trivial phase occurs by the suppression of intralayer Peierls distortion as well.

## Results

### Ultrafast electron diffraction and diffraction pattern of MoTe<sub>2</sub>

The MoTe<sub>2</sub> (and WTe<sub>2</sub>) film used in the experiment is prepared by mechanical exfoliation from a bulk crystal (HQ Graphene). The thickness of the freestanding film on the TEM grid is  $\sim 30$  nm, characterized by the propagation of the breathing phonon mode induced by the laser excitation [26]. A schematic representation of the ultrafast electron diffraction experiment is depicted in Fig. 1c. Visible (550 nm) and midinfrared (2000 nm) femtosecond laser pulses are employed to electronically excite the nanofilm of MoTe<sub>2</sub>. We choose those two pump wavelengths in order to separate the possible contributions of the photoexcitation and the electric field [22, 23] to the structural transition. Another femtosecond electron pulse subsequently probes the structural changes at a varying time delay after the pump laser excitation. The temporal resolution of the system is estimated to be  $\sim 150$  fs (FWHM) [27]. The phase of MoTe<sub>2</sub> in the experiment is controlled by the temperature, i.e. the 1T' phase at room temperature 295 K and the Td phase at 120 K. A prototypical diffraction pattern of the Td phase is shown in Fig. 1d.

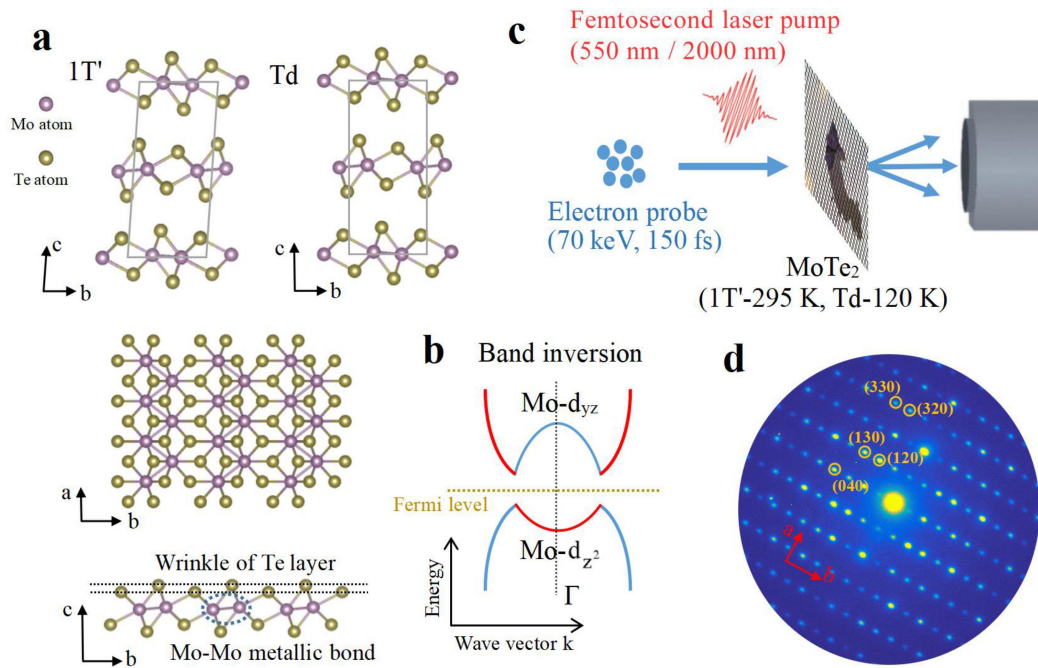


Fig. 1 Crystal structure of MoTe<sub>2</sub> and the diffraction pattern obtained in femtosecond electron diffraction experiment. (a) The unit cells of MoTe<sub>2</sub> in the monoclinic 1T' phase and the orthorhombic Td phase. The bottom are the top view (a-b plane) and the side view (b-c plane) crystal structure of a single layer. The two phases hold the same in-plane crystal structure but different vertical stacking. All the drawings of the crystal structure are produced by VESTA software [28]. (b) Schematic band inversion by intralayer Peierls distortion in monolayer 1T' MoTe<sub>2</sub>. (c) Schematic presentation of the ultrafast electron diffraction experiment. The femtosecond laser pumps the MoTe<sub>2</sub> nanofilm with the crystal phase controlled by the temperature. Another femtosecond electron pulse diffracts off the crystal, thus probing transient structural changes. (d) A prototypical diffraction pattern of MoTe<sub>2</sub> in the experiment. Several spots are labeled by circles.

## Coherent interlayer shear mode in the 1T' phase and the Td phase

To investigate the structural dynamics, we report the relative changes of the Bragg spot intensities as a function of time delay in Fig. 2. For the room temperature 1T' phase, intensity oscillations of the (130) and (120) Bragg spots are observed for both 550 nm and 2000 nm laser excitation, as shown in Fig. 2a. The Fast Fourier Transformation (FFT) amplitude of the oscillation is 0.38 THz, in good agreement with the frequency of the interlayer shear phonon in the Td phase [29]. A recent spectroscopic study reports a similar photoinduced coherent shear phonon in the 1T' phase of MoTe<sub>2</sub> [30]. Two points need to be noticed regarding this shear phonon mode. The first is that the shear phonon mode is Raman inactive in the 1T' phase [29, 31]. The second is that the coherent shear phonon does not occur after THz excitation [22]. The appearance of Raman-inactive phonon modes is generally attributed to lattice symmetry breaking [30, 32]. In the case of 1T' MoTe<sub>2</sub>, an intermediate state with significant structural changes may form and needs to be identified. As the shear phonon mode is silent in the THz photoexcitation [22], the intermediate state is likely be induced by high energy photon excitation.

For the Td phase of MoTe<sub>2</sub>, pronounced intensity oscillations with a frequency of 0.4 THz are observed for both 550 nm and 2000 nm laser excitation as shown in Fig. 2b. This low frequency oscillation with a life time  $\sim 40$  ps is attributed to the interlayer shear phonon mode [23, 29], i.e. the atoms in the same layer vibrate along the same direction while atoms in two adjacent layers vibrate toward opposite directions. The oppositely phased intensity oscillations along the *b* axis (i.e. (h20),

(h30), (h40), (h50)) are shown in Fig. 2c and Fig. S1 in Supplemental Materials, indicating that the intensity oscillations arise from the interlayer shear phonon [22]. A similar shear mode oscillation in the sister compound WTe<sub>2</sub> is also observed and shown in Fig. S2 in Supplemental Materials. In Fig. 2d, a schematic illustration of the interlayer shear displacement is displayed. The interlayer shear mode has been identified as an indication of the structural transition from the Weyl semimetal phase to the trivial semimetal phase [22, 23]. With increasing pump fluence, the amplitude of the shear mode (i.e. the peak-to-peak intensity change) of (130) and (040) increases linearly then saturates somewhat at higher fluence (the threshold fluence is 5.44 mJ/cm<sup>2</sup> with 550 nm laser pump), as shown in Fig. S3 in Supplemental Materials. We simulate the shear displacement induced intensity changes by SingleCrystal [33]. In the simulation, the adjacent layers move in opposite direction along *b* axis by 0.03 Å then -0.03 Å to modulate the shear displacement relative to the equilibrium position. The simulated intensity changes qualitatively agree with the experimental results as shown in Fig. 2e. Note that the pump fluence of 3.81 mJ/cm<sup>2</sup> is close to the threshold fluence of 5.44 mJ/cm<sup>2</sup>, however, the estimated shear displacement is a few picometers, much smaller than the required displacement of ~ 0.19 Å for the symmetry switch [22]. The discrepancy could derive from the limited optical penetration depth, which is estimated to be 50-100 nm [23, 30], causing an inhomogeneous longitudinal excitation over the ~ 30 nm film thickness. Such inhomogeneous excitation is also observed in the THz field pump of WTe<sub>2</sub> [22]. Since the complete symmetry change on the surface layer of MoTe<sub>2</sub> and WTe<sub>2</sub> has been

detected by time-resolved second-harmonic-generation spectroscopy [22, 23], we expect a much larger shear displacement for the few surface layers than the displacement averaged over the 30 nm thickness in our experiments.

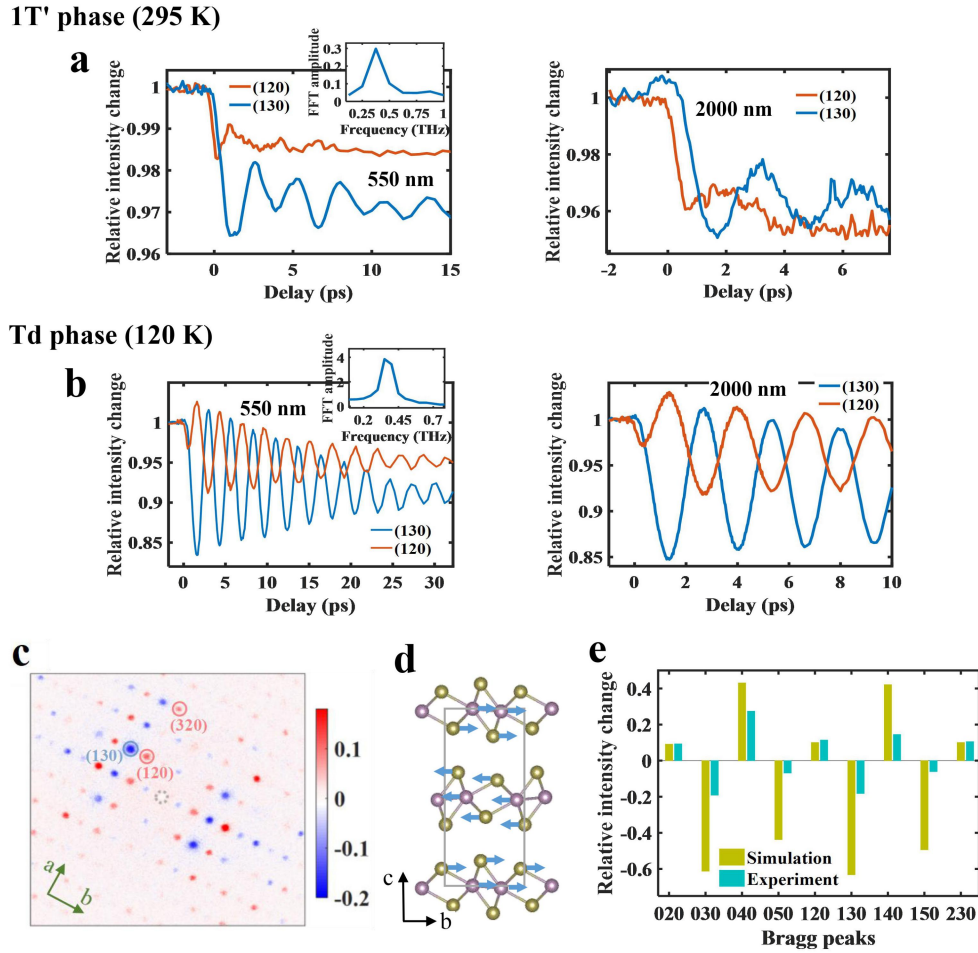


Fig. 2 Photoinduced interlayer shear mode in both 1T' and Td phase of MoTe<sub>2</sub>. (a) For 1T' phase, intensity changes of (130) and (120) with 550 nm (0.84 mJ/cm<sup>2</sup>) and 2000 nm (13.10 mJ/cm<sup>2</sup>) laser pump. The Fast Fourier Transformation (FFT) amplitude of the oscillation in the inset indicates a 0.38 THz shear phonon mode. (b) For Td phase, intensity changes with 550 nm (3.81 mJ/cm<sup>2</sup>) and 2000 nm (15.08 mJ/cm<sup>2</sup>) laser pump. The Fast Fourier Transformation (FFT) amplitude of oscillations in the inset indicates the 0.4 THz shear phonon mode. (c) Difference map of the intensity between the delay points of 1.6 ps and 2.9 ps with 550 (3.81 mJ/cm<sup>2</sup>) nm laser pump. (d) Illustration of the interlayer shear mode. (e) Bar chart showing the shear mode induced intensity changes of several peaks in experiment and simulation.

### **Intralayer structural transition by the reduction of Peierls distortion**

To gain insight into the ultrafast structural response, we focus on the changes of Bragg diffraction intensities in femtosecond timescale. The intensity decay of several Bragg reflections in the 1T' phase is shown in Fig. 3a and 3b for 550 nm and 2000 nm laser pump respectively. Within  $t_1 = 0.3$  ps after photoexcitation, the intensities of the (120), (040) and (130) reflections decay promptly, while the intensities of the (130) and (330) reflections stay unchanged. The same anisotropic intensity changes of these peaks within 0.3 ps is also observed in the Td phase of MoTe<sub>2</sub> (see Fig. 3c and 3d, and Fig. S5 in Supplemental Materials) and the Td phase of WTe<sub>2</sub> (see Fig. S2 in Supplemental Materials). As the pump fluence increases, the intensity decrease of the (130) reflection within 0.3 ps is constant for all fluences, while the intensity change of the (120) reflection continuously increases with fluence as shown in Fig. 3e. The distinct behavior of different Bragg reflections, as shown in Fig. 3, could be a signature of structural transition to an intermediate state instead of Debye-Waller effect. As both the 1T' and Td phases exhibit the same intralayer Peierls distortion, we speculate that the observed anisotropic intensity changes are associated with the reduction of the intralayer Peierls distortion [2], which we will discuss further in the next paragraph. The overall intensity change of every single Bragg reflection is therefore the superposition of the anisotropic intensity change and the shear mode intensity oscillation. Fig. 3f shows that the shear phonon mode in the Td phase is described best by an exponentially decaying cosine function  $A \cos(\omega t + \varphi) \exp(-t/\tau)$ . The frequency  $\omega$  and the phase  $\varphi$  of the best fit are 0.42 THz and -0.04 rad. The

identified cosine oscillation of the shear mode indicates the displacive excitation of this coherent phonon mode (DECP). In this case, the ultrafast electronic excitation gives rise to the immediate change of the potential energy surface and the subsequent harmonic oscillation [34, 35]. Therefore, the reduction of the intralayer Peierls distortion and the interlayer shear mode are probably concurrently excited by the femtosecond laser.

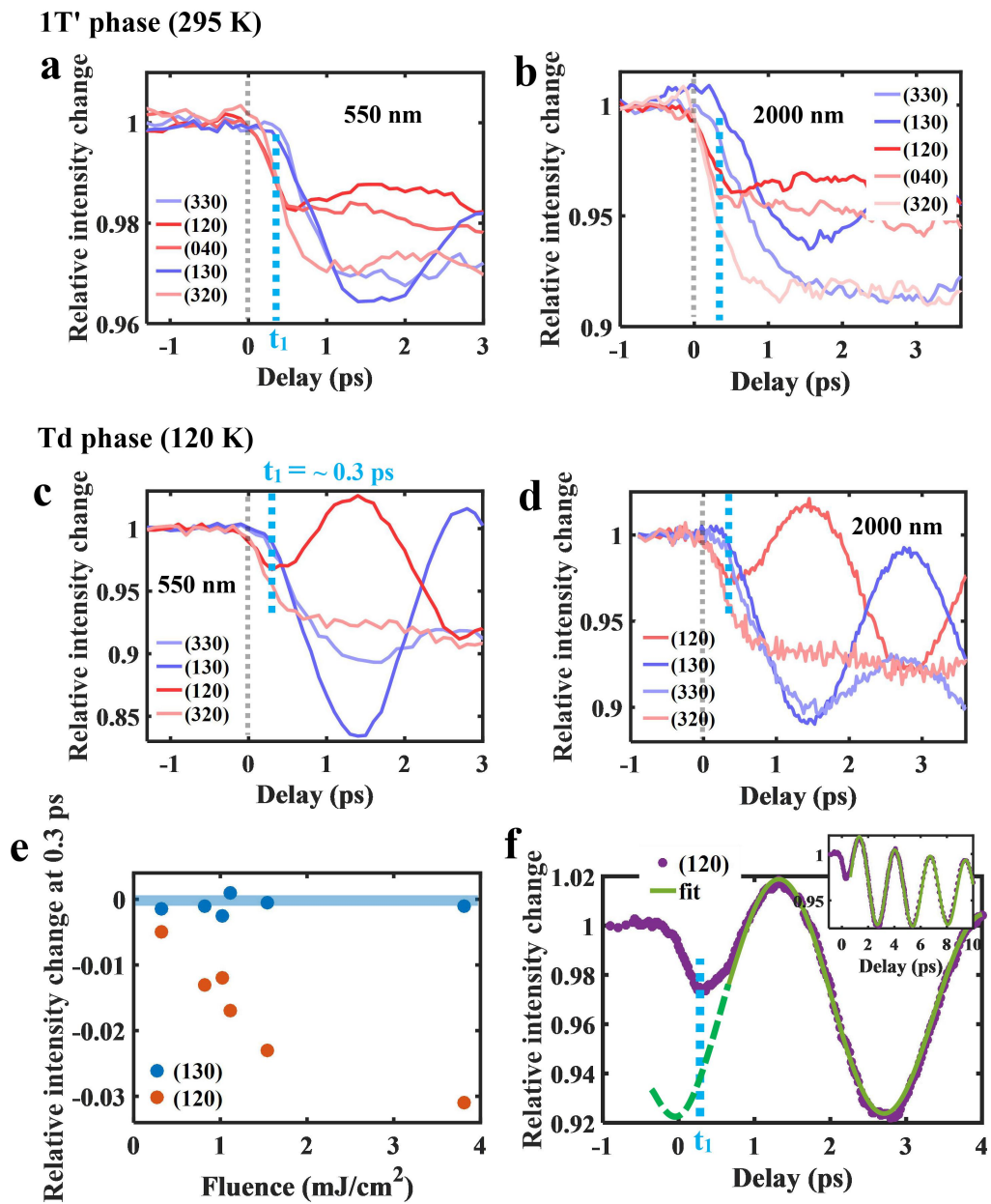


Fig. 3 Ultrafast structural dynamics in both the 1T' and Td phase. (a), (b) Intensity changes in the 1T' phase with 550 nm and 2000 nm laser pump. (c), (d) Intensity changes in the Td phase with 550 nm and 2000 nm laser pump. For both phases, a prompt decay within 0.3 ps ( $t_1$ ) is measured for (120), (040) and (320), while a delay of the intensity decay is observed for (130) and (330). Time traces of (040) in the Td phase are displayed in Fig. S4 in Supplemental Materials. (e) Fluence dependence of the intensity changes in the 1T' phase with 550 nm laser pump at the time delay of 0.3 ps. The intensity of the (120) reflection at this delay stays constant with increasing fluence, while the amplitude of the intensity decay of the (130) reflection continuously increases as the fluence increases. (f) The intensity oscillation of the (120) reflection fitted by an exponentially decaying cosine function (solid green line) with 2000 nm laser pump. The region of the fit covers 0.7 to 10 ps. The dashed green line in the region  $< 0.7$  ps is an extension based on the fit.

For MoTe<sub>2</sub> and WTe<sub>2</sub>, the 1T phase is not stable and the Fermi surface nesting drives the transition to the 1T' phase with the intralayer Peierls distortion [2], characterized by Mo-Mo metallic bonds as well as the out-of-plane wrinkling of Te and Mo atoms as shown in Fig. 4. In general, the femtosecond laser excitation creates non-equilibrium potential energy surfaces, which in many materials releases structural distortions to a high crystal symmetry [36-41]. Examples of such structural phase transition are the ultrafast dissociation of the V-V dimers in VO<sub>2</sub> [38] and Ir-Ir dimers in IrTe<sub>2</sub> [36], and the suppression of periodical lattice distortions in charge density waves systems [40, 41]. In the case of MoTe<sub>2</sub>, the femtosecond laser induces a population in the antibonding d-orbitals of Mo atoms [42, 43], which may give rise to the stretching (and dissociation) of the Mo-Mo metallic bonds. In this circumstance,

the shorter Mo-Mo distance will get elongated as indicated in Fig. 4b by light blue arrows. Based on this concept, we calculate the structure factor and the corresponding diffraction intensity change by Mo-Mo bond stretching in the unit cell of the 1T' phase and the Td phase. The possible reduction of the out-of-plane wrinkling along the c axis is neglected in the subsequent calculation, since the experiment is not sensitive to out-of-plane motions in this geometry. The structure factor is determined by the positions of the atoms in the unit cell,

$$F(hkl) = \sum_j f_j \exp[-2\pi i(hkl) \cdot (xyz)_j] \quad (1)$$

Where  $f_j$  is the atomic scattering factor and the sum is performed over all atoms in the unit cell. The intensity  $I$  of a Bragg reflection  $(hkl)$  is proportional to the amplitude square of the structure factor  $F(hkl)$ , i.e.  $I(hkl) \propto |F(hkl)|^2$ . We simulate the Mo-Mo bond stretching and calculate the corresponding structure factor with SingleCrystal [33]. Fig. 4a and Fig. 4b display the calculated change of  $|F|^2$  as a function of the Mo-Mo bond stretching for the 1T' phase and the Td phase, respectively. The (020), (040), (120) and (320) reflections show a remarkable intensity decrease, while for the (130) and (330) reflections, the intensities remain unchanged or increase slightly. The calculated intensity change of Bragg reflections as a function of Mo-Mo bond distance shows the same trend as the measured change within 0.3 ps in Fig. 3. Therefore, we attribute the ultrafast anisotropic intensity changes to Mo-Mo (W-W) bond stretching in MoTe<sub>2</sub> (WTe<sub>2</sub>).

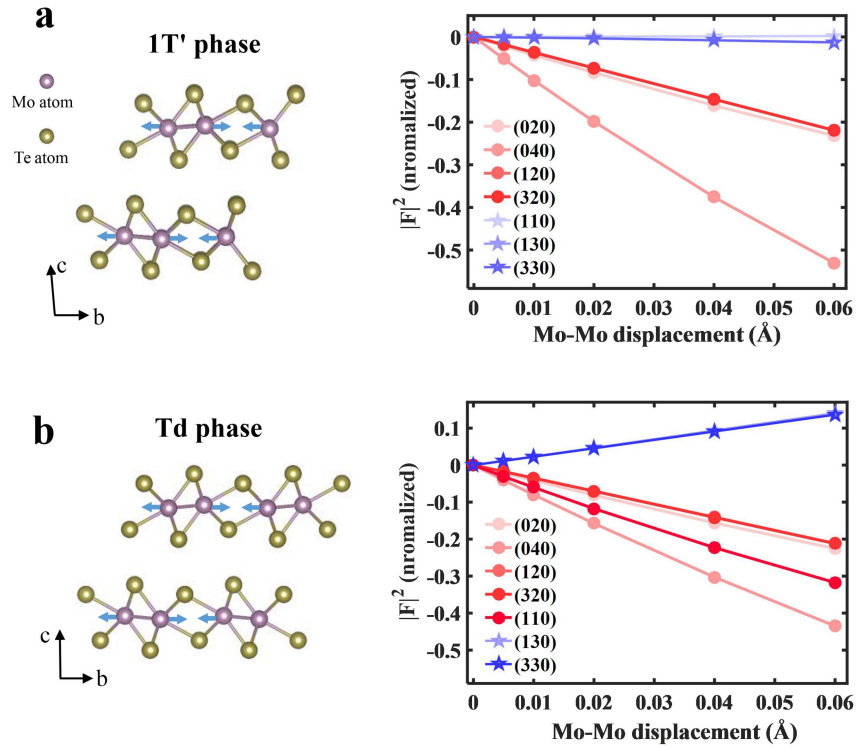


Fig. 4 Simulated Bragg intensity changes in the 1T' and Td phase of MoTe<sub>2</sub> caused by Mo-Mo bond stretching. (a) (left) Schematic illustration of the Mo-Mo bond stretching in the 1T' phase. The Mo-Mo bond (in purple bond color) modulates the adjacent Mo atoms such that the shorter and longer distance alternate. Photoexcitation dissociates the Mo-Mo bond by a directional movement along the b axis indicated by blue arrows. (right) Simulated intensity changes for listed Bragg reflections. In the simulation, the Mo-Mo displacement mimics the bond dissociation along the b axis as indicated in (left). (b) (left) Schematic illustration of the Mo-Mo bond stretching in Td phase. (right) Simulated intensity changes for listed Bragg reflections.

## Photoinduced Intralayer and interlayer atomic motions from TDDFT-MD simulation

To further confirm the concurrent intralayer and interlayer atomic motions, we perform TDDFT-MD simulations for MoTe<sub>2</sub> in its Td phase. The pump fluence is set to 2 mJ/cm<sup>2</sup> close to the experimental condition. More detailed information regarding the simulation can be found in Supplementary Materials. The simulation results are shown in Fig. 5. The arrows in Fig. 5a indicate the directional movements of Mo and Te atoms based on simulated time-dependent displacements in the unit cell. The corresponding displacement trajectories in time for atoms in the middle and the bottom layer are summarized in Fig. 5b-5d and Fig. S6 in Supplementary Materials, respectively. As shown in Fig. 5b (bottom), in the simulations the bond length of Mo1 and Mo2 stretches significantly within ~ 0.3 ps, which agrees with the ultrafast bond stretching from the experimental results (see Fig. 3). Meanwhile, Te8 and Te11 move in opposite directions along the *c* axis as shown in Fig. 5c, which reduces the out-of-plane wrinkling of the Te atoms. The stretching of the metallic bonds and the reduction of the out-of-plane wrinkling of the Te atoms within 0.3 ps evidence the photoinduced suppression of the intralayer Peierls distortion. Note that T8 and Te11 also move simultaneously along the negative direction of *b* axis as shown in Fig. 5c (bottom), while Te7 and Te12 in adjacent layer move along the positive direction of the *b* axis as shown in Fig. S6 in Supplementary Materials. The opposite movements along the *b* axis in these two adjacent layers is a signature of the interlayer shear mode. In Fig. 5d (top), Te10 is on average not moving significantly in comparison with that

of Te5, deviating from the expected shear displacement. This distinction may derive from the dynamical coupling of the interlayer shear mode and the suppression of the intralayer Peierls distortion on ultrafast timescales. The intensity change of several Bragg peaks is calculated based on the atomic displacements at  $T=0.2$  ps in Fig. 5. The calculated anisotropic intensity changes as shown in Fig. S7 in Supplementary Materials, agree qualitatively with the experiment results in Fig. 3. The simulation results in Fig. 5 contains some coherent oscillations of the atomic displacements with the period of 200-300 fs, which are not observed in our experimental results. Such coherent oscillations could be attributed to the excitation of high-frequency ( $\sim 4$  THz) phonon modes [24, 31]. The  $\sim 150$  fs temporal resolution of our experimental system is insufficient to detect such ultrafast oscillations.

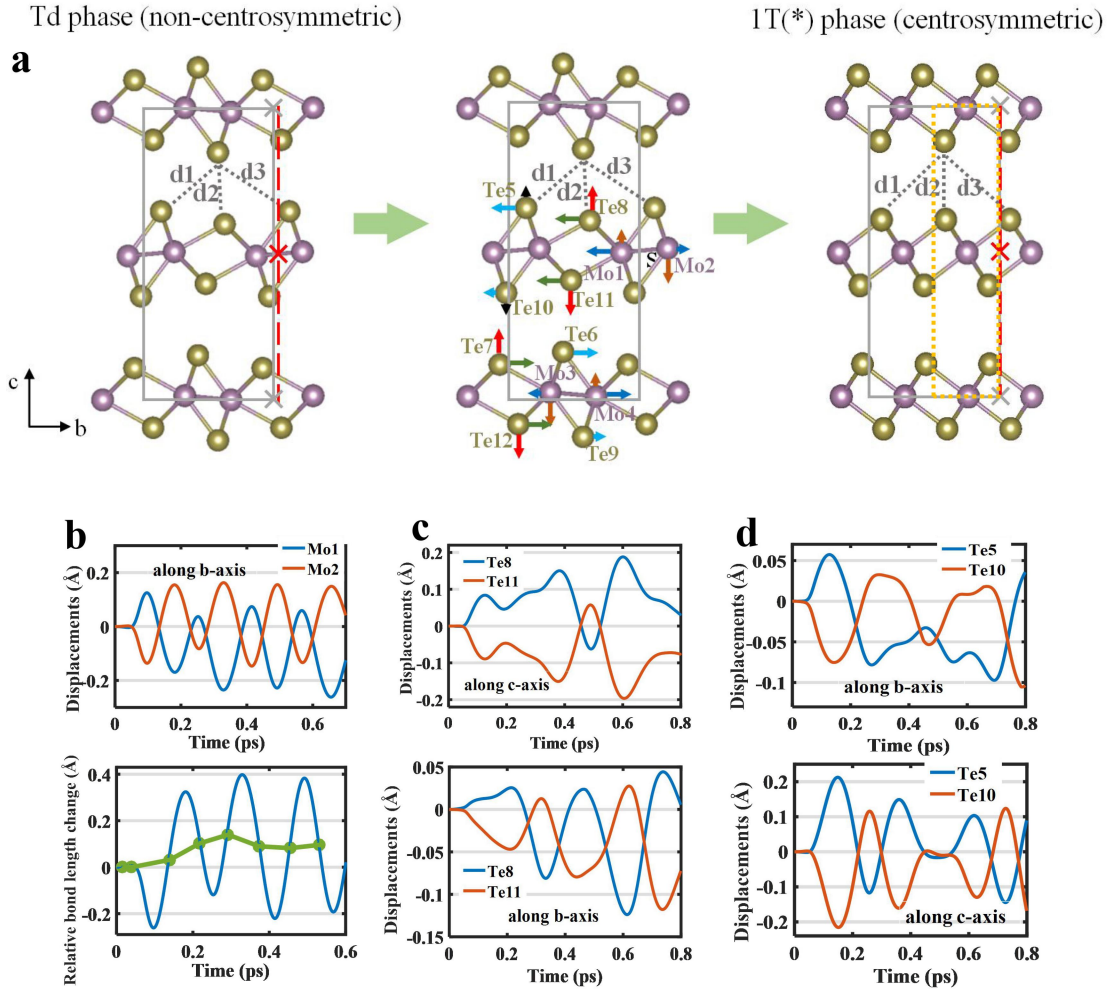


Fig. 5 Transient atomic motions after femtosecond laser excitation by TDDFT-MD simulations. (a) In-plane and out-of-plane movements of Mo and Te atoms indicated by arrows after the laser excitation. The gray rectangle is the unit cell of the Td phase. The gray crosses are symmetry centers of top and bottom layers and the red cross is the symmetry center of the middle layer. An intermediate state 1T(\*) is formed with an intralayer structure akin to the undistorted 1T phase. The bond length  $d_3 > d_1$  in the Td phase, while  $d_3 = d_1$  in the 1T(\*) phase. The dotted yellow rectangular indicates the unit cell of the 1T(\*) phase. (b) The time-dependent displacements of Mo1 and Mo2 along the b axis. The blue curve in the bottom figure shows the metallic bond length changes between Mo1 and Mo2. The green dots are the average of the adjacent peak-to-peak values. (c) The time-dependent displacements of Te8 and Te11 along the c axis and b axis. (d) The time-dependent displacements of Te5 and Te10 along the b axis and c axis.

The simulation results in Fig. 5 unambiguously demonstrate the concurrent interlayer shear displacement and the suppression of intralayer Peierls distortion, in good agreement with the experiment results. A schematic illustration of the structural changes based on these two dynamical processes is summarized in Fig. 5a. On sub-ps timescales, the intralayer distortion is suppressed to a 1T-like structure. Meanwhile, the shear displacement reduces the bond length discrepancy between  $d_1$  and  $d_3$  and the interlayer stacking is changed correspondingly as shown in Fig. 5a. When the symmetry center of the top (bottom) layer (i.e. the gray crosses) gets aligned to that of the center layer (i.e. the red cross), a structural transition from the non-centrosymmetric to the centrosymmetric can be achieved by the shear displacement. We define an intermediate centrosymmetric 1T(\*) phase with 1T-like intralayer structure (Fig. 5a (right)). Therefore, the photoexcitation induces a structural transformation from the non-centrosymmetric Td phase (Fig. 5a (left)) to the centrosymmetric 1T(\*) phase (Fig. 5a (right)). Note that the unit cell of the 1T(\*) phase indicated by the dotted rectangular, as shown in Fig. 5a (right), will be half of the unit cell of the Td phase (the gray rectangle) along the  $b$  axis, which may be a signature for further experimental study on the structural transition. In our experiment, the inhomogeneous longitudinal excitation due to the limited optical penetration depth may blur the underlying unit cell change.

## Discussion

The pathway of the concurrent intralayer and interlayer structural transitions in

real space and the sketch of the modulation of the potential energy surface by photoexcitation for the Td phase of MoTe<sub>2</sub> is illustrated in Fig. 6. After photoexcitation, the occupation of the antibonding d-orbitals of Mo atoms induces the stretching of the in-plane metallic Mo-Mo bonds. It is conceivable that at higher pump fluence, the Mo-Mo bond will dissociate completely. The Mo-Mo bonds stretching and the reduction of the out-of-plane wrinkling of Te atoms give rise to an ultrafast suppression of the Peierls distortion and a transition to intralayer 1T-like structure within 0.3 ps. Meanwhile, the interlayer shear displacement produces a coherent shear phonon mode at moderate excitation density and a transition to a centrosymmetric phase in sub-period of the shear phonon mode at high excitation density. The corresponding modulations of the potential energy surface along the Peierls distortion coordinate and the shear mode coordinate are shown in Fig. 6b and 6c respectively. For the 1T' phase of MoTe<sub>2</sub>, the same intralayer structural transition (i.e. the suppression of intralayer Peierls distortion) by photoexcitation as that in the Td phase is identified. It is surprising that the Raman-inactive shear mode is observed in 1T' phase. The same shear mode in the 1T' phase is also observed in femtosecond optical pump-probe reflectivity [30], which suggests that it is not caused by the possible interlayer stacking fault. A simple question is that if there is any correlation between the intralayer and interlayer structural transitions in both the 1T' phase and the Td phase. The excitation of the Raman-inactive shear mode in the 1T' phase may suggest a certain facilitation of the intralayer structural transition to the interlayer shear mode, which needs to be studied further.

The significance of the findings in our work are multifold. First, the concurrent intralayer and interlayer structural transitions is the intrinsic mechanism for the visible and infrared femtosecond laser induced Weyl semimetal phase to trivial phase transition [23]. Second, the ultrafast intralayer structural transition and the dispersive excitation of the shear phonon mode indicate that the electron-phonon coupling is the driving force of the topological switching, which is distinct from the THz/light field driven topological switching in Ref. 22-24. The same structure response under 550 nm and 2000 nm laser excitation suggests such photoexcitation induced topological switching in a wide spectrum range. Third, the intralayer Peierls distortion causes the band inversion [2, 17, 14], therefore, the topological insulator phase in monolayer [2, 4, 5, 17] and the higher-order topological insulator phase in bulk 1T' and Td phase [13, 14, 16] are expected to switch to the trivial phase upon suppression of the intralayer Peierls distortion. Moreover, the quantum spin Hall state based on the topological band inversion in monolayer 1T' WTe<sub>2</sub> and MoTe<sub>2</sub> [4-7] will also be modulated by the suppression of the intralayer Peierls distortion. Fourth, the ultrafast suppression of the intralayer Peierls distortion can be used to tune the anisotropic electronic and optical properties in the 1T' phase of TMDCs for specific applications [25].

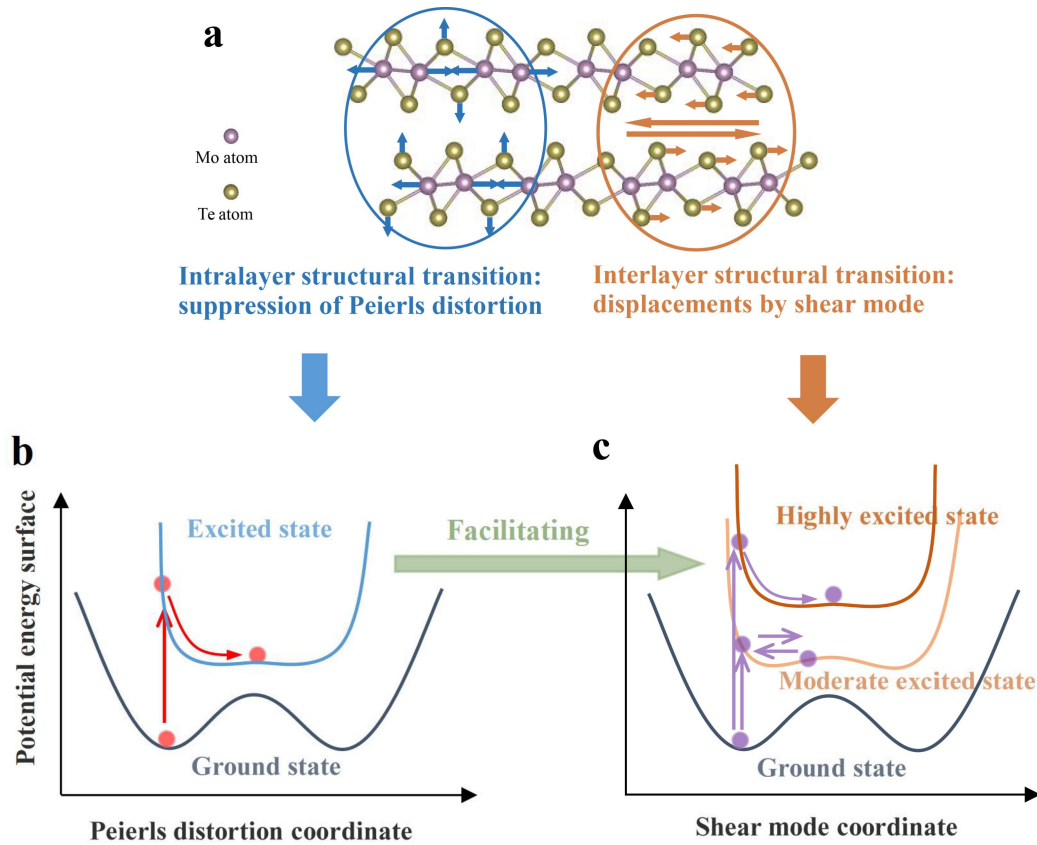


Fig. 6 Schematic presentation of the photoinduced intralayer and interlayer structural transitions in real space and the corresponding changes of the potential energy surface in the 1T' and the Td phase of MoTe<sub>2</sub>. (a) Intralayer structural transition by suppression of the Peierls distortion and interlayer structural transition by shear mode. The main atomic motions include the dissociation of Mo-Mo bonds and the reduction of the out-of-plane wrinkling of Te atoms for the intralayer transition, and the interlayer shear displacement for the interlayer transition. (b) The potential energy surface of the Peierls distortion modulated by photoexcitation. The flattened potential energy surface after photoexcitation gives rise to the suppression of Peierls transition to an 1T-like intralayer structure. (c) The potential energy surface of the shear mode after photoexcitation. At low excitation density, a coherent shear phonon mode is excited. At high excitation density, the symmetry switches from noncentrosymmetry to centrosymmetry in a sub-period of the shear phonon mode. The green arrow indicates a possible facilitation effect of the intralayer structural transition to the interlayer structural transition.

In conclusion, we reveal photoexcitation induced concurrent intralayer and interlayer structural transitions in the 1T' and the Td phase of MoT<sub>2</sub> and WTe<sub>2</sub> by femtosecond electron diffraction and TDDFT-MD simulations. The multifold topological nontrivial to trivial transitions based on the ultrafast intralayer and interlayer structural transitions are discussed. The ultrafast stretching and dissociation of metallic Mo-Mo (W-W) bonds and the suppression of the intralayer Peierls distortion brings new insights to the ultrafast manipulation of electronic structures and anisotropic electronic/optical properties [25]. Moreover, as the 1T' phase, instead of 1T phase, is the room temperature stable phase in most monolayer TMDCs [25], the photoinduced suppression of the intralayer Peierls distortion and the associated modulation of the electronic structure are expected to occur in most monolayer TMDCs.

## **Acknowledgements**

This work was funded by the Max Planck Society and the European Research Council (ERC) under the European Union's Horizon 2020 research and innovation program (Grant Agreement Number ERC-2015-CoG-682843). Yingpeng Qi acknowledges support by the Sino-German (CSC-DAAD) Postdoc Scholarship Program (Grant No. 201709920054 and No. 57343410) and the funding from Max Planck Society. Yingpeng Qi acknowledges Jianming Cao from Shanghai Jiao Tong University for providing the simulation software of SingleCrystal.

## References

1. Wang, Y., Xiao, J., Zhu, H., Li, Y., Alsaied, Y., Fong, K. Y., Zhou, Y., Wang, S., Shi, W., Wang, Y., Zettl, A., Reed, E. J. & Zhang, X. Structural phase transition in monolayer MoTe<sub>2</sub> driven by electrostatic doping. *Nature* **550**, 487 (2017).
2. Keum, D., Cho, S., Kim J., Choe, D., Sung, H., Kan M., Kang H., Hwang J., Kim, S., Yang, H., Chang, K. and Lee, Y. Bandgap opening in few-layered monoclinic MoTe<sub>2</sub>. *Nat. Phys.* **11**, 482 (2015).
3. Ali, M., Xiong, J., Flynn, S., Tao, J., Gibson, Q., Schoop, L., Liang, T., Haldolaarachchige, N., Hirschberger, M., Ong, N., Cava, R. Large, non-saturating magnetoresistance in WTe<sub>2</sub>. *Nature* **514**, 205–208 (2014).
4. Qian, X., Liu J., Fu L., Li, J. Quantum spin Hall effect in two-dimensional transition metal dichalcogenides. *Science* **346**, 1344 (2014).
5. Tang, S., Zhang, C., Wong, D. et al. Quantum spin Hall state in monolayer 1T'-WTe<sub>2</sub>. *Nat. Phys.* **13**, 683 (2017).
6. Fei, Z. et al. Edge conduction in monolayer WTe<sub>2</sub>. *Nat. Phys.* **13**, 677 (2017).
7. Wu, S. et al. Observation of the quantum spin Hall effect up to 100 kelvin in a monolayer crystal. *Science* **359**, 76 (2018).
8. Deng, K. et al. Experimental observation of topological Fermi arcs in type-II Weyl semimetal MoTe<sub>2</sub>. *Nat. Phys.* **12**, 1105-1110 (2016).
9. Tamai, A. et al. Fermi arcs and their topological character in the candidate type-II Weyl semimetal MoTe<sub>2</sub>. *Phys. Rev. X* **6**, 031021 (2016).

10. Huang, L. et al. Spectroscopic evidence for a type II Weyl semimetallic state in MoTe<sub>2</sub>. *Nat. Mater.* **15**, 1155–1160 (2016).
11. Jiang, J. et al. Signature of type-II Weyl semimetal phase in MoTe<sub>2</sub>. *Nat. Commun.* **8**, 13973 (2017).
12. Soluyanov, A., Gresch, D., Wang, Z., Wu Q., Troyer, M., Dai, X. & Bernevig, B. Type-II Weyl semimetals. *Nature* **527**, 495 (2015).
13. Tang, F., Po, H., Vishwanath, A. and Wan, X. Efficient topological materials discovery using symmetry indicators. *Nat. Phys.* **15**, 470 (2019).
14. Wang, Z., Wieder, B., Li, J., Yan, B., and Bernevig, B. Higher-Order Topology, Monopole Nodal Lines, and the Origin of Large Fermi Arcs in Transition Metal Dichalcogenides XTe<sub>2</sub> (X =Mo;W). *Phys. Rev. Lett.* **123**, 186401 (2019).
15. Li, P. et al. Evidence for topological type-II Weyl semimetal WTe<sub>2</sub>. *Nat. Commun.* **8**, 2150 (2017).
16. Choi, Y., Xie, Y., Chen, C. et al. Evidence of higher-order topology in multilayer WTe<sub>2</sub> from Josephson coupling through anisotropic hinge states. *Nat. Mater.* **19**, 974-979 (2020).
17. Choe, D., Sung, H., and Chang, K. J. Understanding topological phase transition in monolayer transition metal dichalcogenides, *Phys. Rev. B* **93**, 125109 (2016).
18. Senthil, T. Symmetry-Protected Topological Phases of Quantum Matter. *Annu. Rev. Condens. Matter Phys.* **6**, 299-324 (2015).
19. Tang, F., Po, H., Vishwanath, A. & Wan, X. Comprehensive search for topological materials using symmetry indicators. *Nature* **566**, 486-489(2019).

20. Vergniory, M., Elcoro, L., Felser, C., Regnault, N., Bernevig, B. & Wang, Z. A complete catalogue of high-quality topological materials. *Nature* **566**, 480-485(2019).
21. Zhang, T., Jiang, Y., Song, Z., Huang, H., He, Y., Fang, Z., Weng, H., Fang, C. Catalogue of topological electronic materials. *Nature* **566**, 475-479 (2019).
22. Sie, E. et al. An ultrafast symmetry switch in a Weyl semimetal. *Nature* **565**, 61 (2019).
23. Zhang, M. et al. Light-Induced Subpicosecond Lattice Symmetry Switch in MoTe<sub>2</sub>. *Phys. Rev. X* **9**, 021036 (2019).
24. Hein, P., Jauernik, S., Erk, H. et al. Mode-resolved reciprocal space mapping of electron-phonon interaction in the Weyl semimetal candidate Td-WTe<sub>2</sub>. *Nat Commun* **11**, 2613 (2020).
25. Chi Sin Tang, Xinmao Yin and Andrew T. S. Wee, 1D chain structure in 1T'-phase 2D transition metal dichalcogenides and their anisotropic electronic structures, *Appl. Phys. Rev.* **8**, 011313 (2021).
26. Chatelain, R., Morrison, V., Klarenaar, B. and Siwick, B. Coherent and incoherent electron-phonon coupling in graphite observed with radio-frequency compressed ultrafast electron diffraction. *Phys. Rev. Lett.* **113**, 235502 (2014).
27. Waldecker, L., Bertoni, R., and Ernstorfer, R. Compact femtosecond electron diffractometer with 100 keV electron bunches approaching the single-electron pulse duration limit. *J. Appl. Phys.* **117**, 044903 (2015).
28. Momma, K. and Izumi, F. VESTA 3 for three-dimensional visualization of crystals,

- volumetric and morphology data, *J. Appl. Crystallogr.* **44**, 1272-1276 (2011).
29. Zhang, K. et al. Raman signatures of inversion symmetry breaking and structural phase transition in type-II Weyl semimetal MoTe<sub>2</sub>. *Nat. Commun.* **7**, 13552 (2016).
30. Fukuda, T., Makino, K., Saito, Y., Fons, P., Kolobov, A., Ueno, K. and Hase, M. Ultrafast dynamics of the low frequency shear phonon in 1T' - MoTe<sub>2</sub>. *Appl. Phys. Lett.* **116**, 093103 (2020).
31. Chen, S. et al. Activation of New Raman Modes by Inversion Symmetry Breaking in Type II Weyl Semimetal Candidate T'-MoTe<sub>2</sub>. *Nano Lett.* **16**, 5852–5860 (2016).
32. Yamamoto, M. et al. Strong Enhancement of Raman Scattering from a Bulk-Inactive Vibrational Mode in Few-Layer MoTe<sub>2</sub>. *ACS Nano* **8**, 3903 (2014).
33. CrystalMaker Software Limited, SingleCrystal 4.0. Available at: <http://www.crystallmaker.com>.
34. Bothschafter, E. et al. Ultrafast Evolution of the Excited-State Potential Energy Surface of TiO<sub>2</sub> Single Crystals Induced by Carrier Cooling. *Phys. Rev. Lett.* **110**, 067402 (2013).
35. Zeiger, H. J., Vidal, J., Cheng, T. K., Ippen, E. P., Dresselhaus, G., Dresselhaus, M. S., Theory for displacive excitation of coherent phonons. *Phys. Rev. B* **45**, 768 (1992).
36. Ideta, S.-i., Zhang, D., Dijkstra, A. G., Artyukhin, S., Keskin, S., Cingolani, R., Shimojima, T., Ishizaka, K., Ishii, H., Kudo, K., Nohara, M., Miller, R. J. D.

- Ultrafast dissolution and creation of bonds in IrTe<sub>2</sub> induced by photodoping. *Sci. Adv.* **4**, eaar3867 (2018).
37. Frigge, T., Hafke, B., Witte, T. et al. Optically excited structural transition in atomic wires on surfaces at the quantum limit. *Nature* **544**, 207–211 (2017).
38. Wall, S., Yang, S., Vidas, L. et al. Ultrafast disordering of vanadium dimers in photoexcited VO<sub>2</sub>. *Science* **362**, 572 (2018).
39. Sokolowski-Tinten, K., Blome, C., Blums, J. et al. Femtosecond X-ray measurement of coherent lattice vibrations near the Lindemann stability limit. *Nature* **422**, 287–289 (2003).
40. Eichberger, M., Schäfer, H., Krumova, M. et al. Snapshots of cooperative atomic motions in the optical suppression of charge density waves. *Nature* **468**, 799 (2010).
41. Haupt, K., Eichberger, M., Erasmus, N., Rohwer, A., Demsar, J., Rossnagel, K., Schwoerer, H. Ultrafast Metamorphosis of a Complex Charge-Density Wave. *Phys. Rev. Lett.* **116**, 016402 (2016).
42. Mar, A., Jovic, S., Ibers, J. A. Metal-Metal vs Tellurium-Tellurium Bonding in WTe<sub>2</sub> and Its Ternary Variants TaIrTe<sub>4</sub> and NbIrTe<sub>4</sub>, *J. Am. Chem. Soc.* **114**, 23 (1992).
43. Canadell, E., LeBeuze, A., Khalifa, M. A. E., Chevrel, R., Whangbo, M. H. Origin of metal clustering in transition-metal chalcogenide layers MX<sub>2</sub> (M = Nb, Ta, Mo, Re; X = S, Se). *J. Am. Chem. Soc.* **111**, 3778 (1989).

## Supplemental Materials

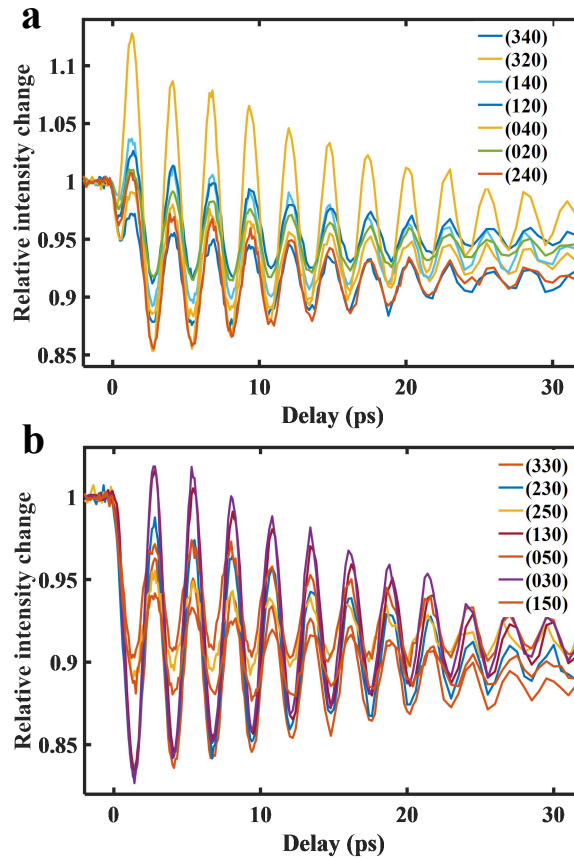


Fig. S1 Intensity oscillation of Bragg spots modulated by the shear phonon mode in the Td phase of MoTe<sub>2</sub>. The pump laser is 550 nm and 3.81 mJ/cm<sup>2</sup>. The intensities of (h20) and (h40) in (a) oscillate in the opposite phase of (h30) and (h50) in (b). The alternate, oppositely phased intensity oscillation along the *b* axis indicates the intensity modulation arises from the interlayer shear phonon along the *b* axis.

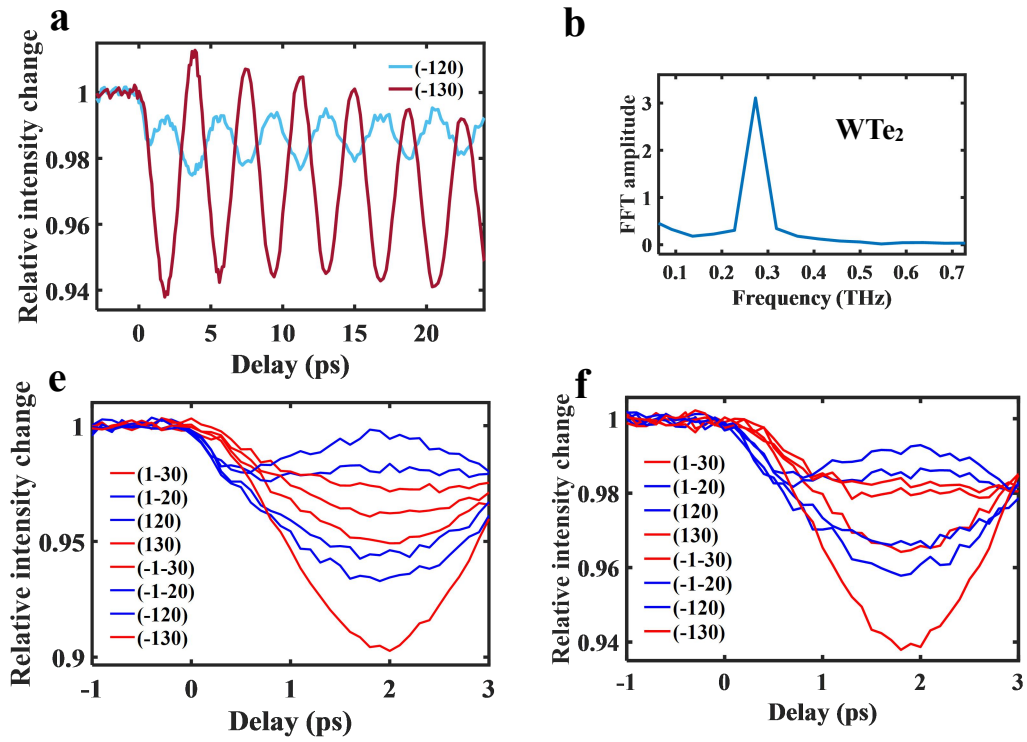


Fig. S2 Anisotropic intensity modulations and time-delayed intensity changes in  $\text{WTe}_2$ . (a), (b) Shear mode oscillations by 500 nm ( $1.08 \text{ mJ/cm}^2$ ) laser pump. The FFT amplitude of the oscillation indicates a frequency of 0.27 THz. (c), (d) Anisotropic intensity modulations for  $\{130\}$  and  $\{120\}$  in  $\text{WTe}_2$  by 550 nm ( $1.08 \text{ mJ/cm}^2$ ) laser pump. (e), (f) Time traces of  $\{120\}$  and  $\{130\}$  with (a) 550 nm ( $1.77 \text{ mJ/cm}^2$ ) and (b)  $1.08 \text{ mJ/cm}^2$  laser pump, both of which show a prompt intensity decay of  $\{120\}$  and an apparent time-delayed intensity change of  $\{130\}$ .

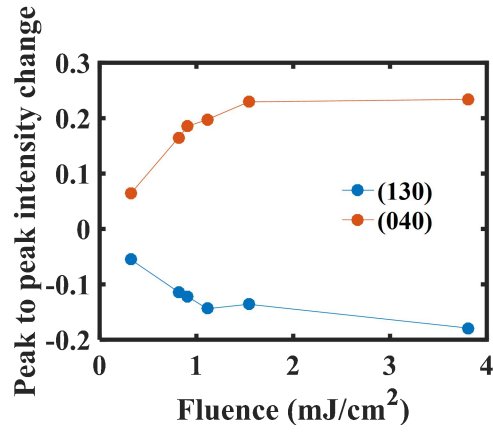


Fig. S3 Peak-to-peak intensity change of (130) and (040) on pump fluence for the Td phase of MoTe<sub>2</sub>. The pump laser is 550 nm.

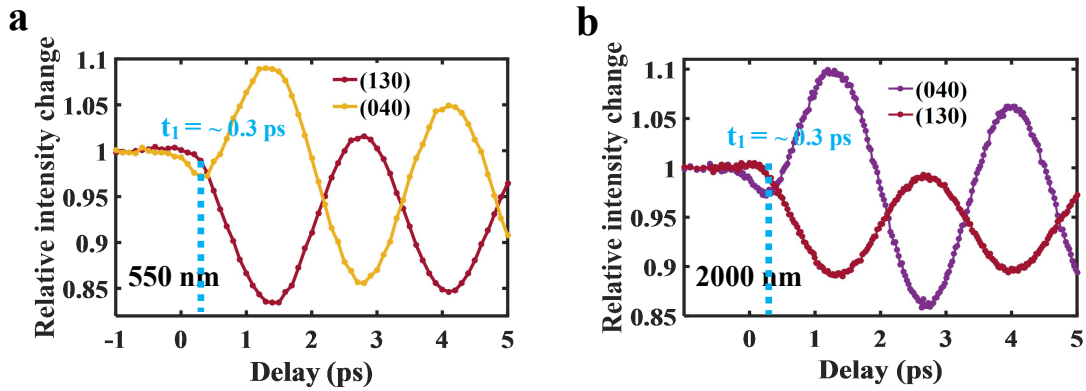


Fig. S4 (a), (b) Time traces of intensity changes at the Td phase of MoTe<sub>2</sub> with 550 nm (3.81 mJ/cm<sup>2</sup>) and 2000 nm (15.08 mJ/cm<sup>2</sup>) laser pump respectively. A prompt decay within 0.3 ps is measured for (040), while a time-delayed intensity decay is observed for (130).

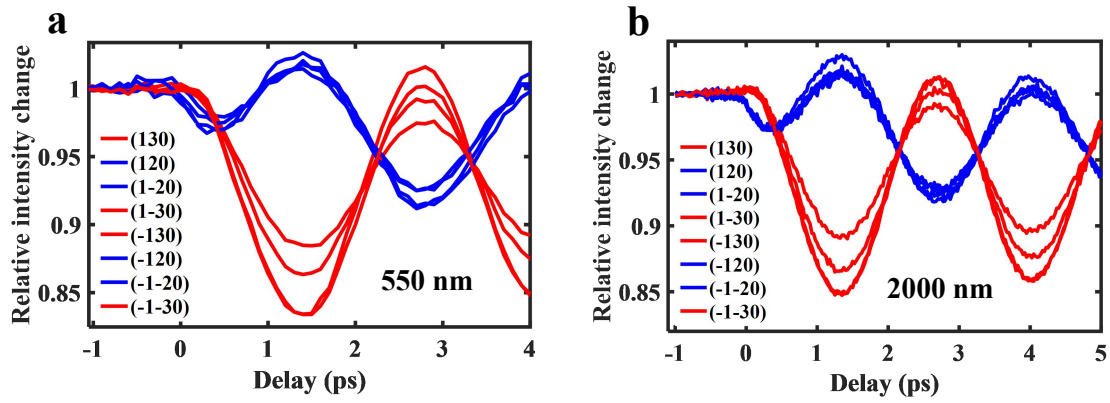


Fig. S5 Time traces for intensity changes of {120} and {130} at the Td phase of MoTe<sub>2</sub> with (a) 550 nm (3.81 mJ/cm<sup>2</sup>) laser pump and (b) 2000 nm (15.08 mJ/cm<sup>2</sup>) laser pump. On sub-ps timescales, both figures show apparent time-delayed intensity decay of the {130} in contrast to the instantaneous intensity decay of the {120} after photoexcitation.

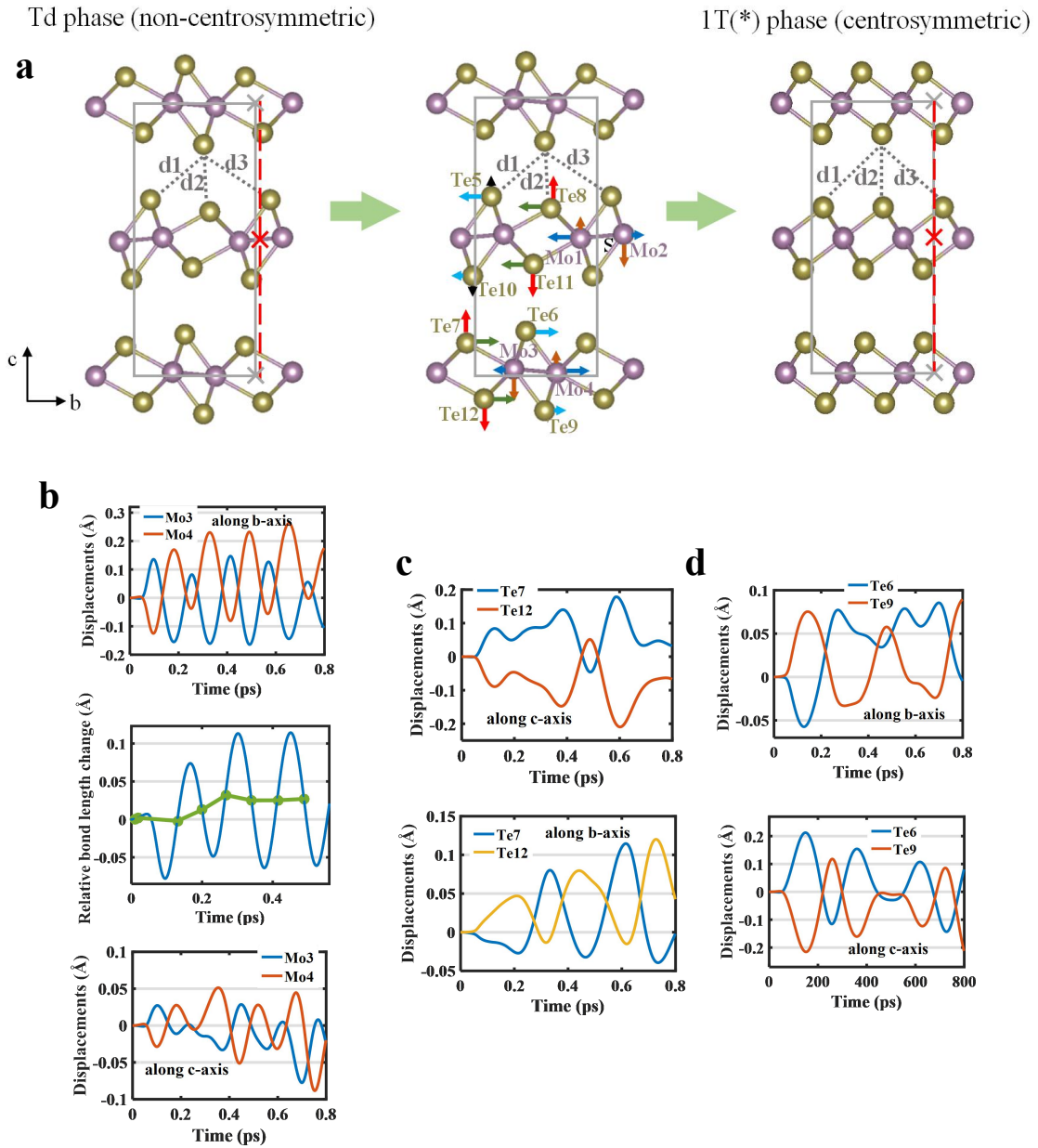


Fig. S6 Simulated atomic motions in the bottom layer of the unit cell. (a) In-plane and out-of-plane movements of Mo and Te atoms indicated by arrows after the laser excitation. (b) Time-dependent displacements of Mo3 and Mo4 along the  $b$  axis and  $c$  axis. The blue curve in the middle figure is metallic bond length changes between Mo3 and Mo4. The green dots are the average of the adjacent peak-peak values. (c) Time-dependent displacements of Te7 and Te12 along the  $c$  axis and  $b$  axis. (d) Time-dependent displacements of Te6 and Te9 along the  $b$  axis and  $c$  axis.

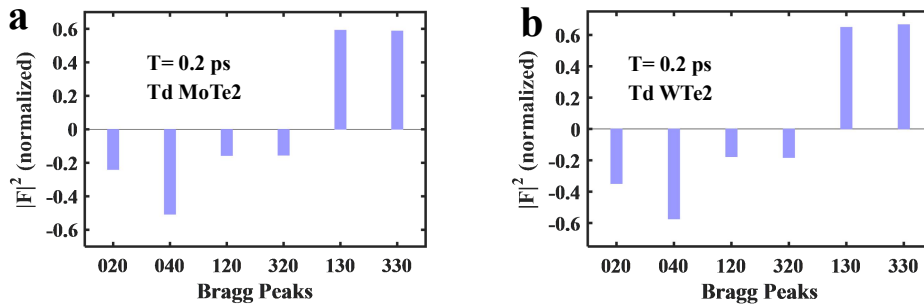


Fig. S7 Bar charts showing calculated intensity changes of Bragg reflections based on simulated atomic displacement at  $T = 0.2$  ps in Fig. 5. The structure factor is calculated by SingleCrystal. For both Td phase of MoTe<sub>2</sub> and WTe<sub>2</sub>, (020), (040), (120), (320) show intensity decrease while (130) and (330) show intensity increase, agree qualitatively with the experiment results in Fig. 3 and Fig. S2. The discrepancy between the calculated intensity change and the experiment results, such as the percentage and remained (130) and (330) intensity in experiment VS significant intensity increase of (130) and (330) in calculation, may derive from the inhomogeneous longitudinal excitation due to limited optical penetration depth in experiment, and the TDDFT-MD simulation method.

## Methods for TDDFT-MD simulations

The experimental geometry of the bulk MoTe<sub>2</sub> is adopted, which is characterized by an orthorhombic (T<sub>d</sub>) unit cell without inversion symmetry [1]. To study the optoelectronic responses of MoTe<sub>2</sub> in T<sub>d</sub> phase, linearly polarized laser beams with time-dependent electric field  $E(t) = E_0 \cos(\omega t) \exp[-(t-t_0)^2/2\sigma^2]$  are applied along the crystallographic a-axis. The photon energy, width, and amplitude are set as 2.25 eV ( $\lambda = 550$  nm), 15 fs and 0.06 V/Å, respectively. This setup allows us to reproduce a laser fluence (ca. 2 mJ/cm<sup>2</sup>) similar to experimental measurements.

The TDDFT-MD calculations are performed using the time dependent ab initio package (TDAP) as implemented in SIESTA [2-4]. The bulk MoTe<sub>2</sub> in its T<sub>d</sub> phase is simulated with a unit cell of 12 atoms with periodical boundary conditions. Numerical atomic orbitals with double zeta polarization (DZP) are employed as the basis set. The electron-nuclear interactions are described by Troullier-Martins pseudopotentials, PBE functional [5]. An auxiliary real-space grid equivalent to a plane-wave cutoff of 250 Ry is adopted. To make a good balance between the calculation precision and cost, a  $\Gamma$ -centered  $6 \times 5 \times 3$  k-point grid is used to sample the Brillouin zone. The coupling between atomic and electronic motions is governed by the Ehrenfest approximation [6]. During dynamic simulations the evolving time step is set to 0.05 fs for both electrons and ions in a micro-canonical ensemble.

1. Qi, Y. *et al.* Superconductivity in Weyl semimetal candidate MoTe<sub>2</sub>, *Nat Commun* **7**, 11038 (2016).

2. Meng, S., Kaxiras, E. Real-time, local basis-set implementation of time-dependent density functional theory for excited state dynamics simulations, *J. Chem. Phys.* **129**, 054110 (2008).
3. Ma, W., Zhang, J., Yan, L., Jiao, Y., Gao, Y., Meng, S. Recent progresses in real-time local-basis implementation of time dependent density functional theory for electron–nucleus dynamics, *Comp. Mater. Sci.* **112**, 478 (2016).
4. Lian, C., Guan, M., Hu, S., Zhang, J., Meng, S. Photoexcitation in Solids: First - Principles Quantum Simulations by Real - Time TDDFT, *Adv. Theory. Simul.* **1**, 1800055 (2018).
5. Perdew, J. P., Burke, K., Ernzerhof, M. Generalized Gradient Approximation Made Simple, *Phys. Rev. Lett.* **77**, 3865 (1996).
6. Alonso, J. L., Andrade, X., Echenique, P., Falceto, F., Prada-Gracia, D., and Rubio, A. Efficient formalism for large-scale ab initio molecular dynamics based on time-dependent density functional theory, *Phys. Rev. Lett.* **101**, 096403 (2008).